**ORIGINAL PAPER**

# Effect of Ni–P content on microstructure and mechanical properties of Fe–Ni–P alloy

Chi Liu[1,2] · Yu-xuan Liu[1] · Ji-ping Lu[1,2] · Yan-huan Wang[1,2] · Lin-wang Chen[1] · Cheng-song Zhang[1,2] · Da-zhi Chen[1,2] · Guo-dong Cui[1,2]

**Abstract**

A series of Fe–Ni–P alloys with different Ni–P contents were prepared by micro-press sintering, and the influence of the contents on the final microstructure and mechanical properties was evaluated. Sample Fe–34(Ni, P) contains the highest Ni–P content (34.18 wt.%) and its relative density reaches 98.75%, which is attributed to the introduction of an appropriate amount of liquid phase during the sintering process. The main phase of the sample is transformed from $\alpha$ to $\gamma$ phase under the gradual increment of Ni–P content. Simultaneously, a large number of phosphides that have strong inhibition on the migration and expansion of grain boundaries are precipitated on the matrix, and synergistic effect with low-temperature sintering results in partial grain refinement. The samples with high Ni–P content have a high volume of $\gamma$ phase, which makes the sample show the optimal plasticity under the maximum compressive load. And the fracture mode has also changed from brittle fracture to a mixed mode of brittle and ductile fracture. The decrease in the proportion of $\alpha$ phase has a weakening effect on the strength, but the refinement of the grain and the increase in the phosphide are the factors that increase the strength, so that the degree of manifestation varies in different Ni–P levels.

**Keywords** Fe–Ni–P alloy · Liquid phase sintering · Mechanical behavior · Microstructure

## 1 Introduction

Fe–Ni binary alloy with face-centered cubic microstructure plays an important role in the field of magnetic materials due to their excellent soft magnetic properties [1, 2]. In the past few decades, its soft magnetic properties have been extensively studied and applied to many fields [3–5]. Although soft magnetic metals have excellent magnetic properties and plasticity, people have never stopped exploring their mechanical properties owing to their limited strength and hardness [6]. Adding alloying elements to iron-based powder metallurgy materials through alloying can improve their mechanical properties without significantly reducing their magnetic properties [7]. The traditional theory believes that phosphorus (P) is regarded as an impurity element in metals because it will segregate at the grain boundary and make the grain boundary embrittlement may have an opposite effect to the ideal [8]. The role of P in the alloy is not necessarily all harmful, and it also has a beneficial aspect to the toughness [9].

Recently, Fe–Ni–P composite powder prepared by electroless Ni–P plating has excellent mechanical properties after sintering [7, 10]. Electroless plating makes the plating solution of the related elements deposited into the alloy with the help of appropriate reducing agents while its good uniformity and practicability are favored by consumers gradually [11, 12]. The minimum temperature of the liquid phase produced during the sintering process is determined by the eutectic temperature (891 °C) in Ni–P binary phase diagram [13], while low-temperature sintering can effectively avoid coarse grain size, and hard and brittle eutectic microstructure. The local density during sintering is related to Ni–P inclusions [14], while high temperatures

✉ Guo-dong Cui
gdcui@swjtu.edu.cn

1 Key Laboratory of Advanced Technology of Materials of Education Ministry, School of Materials Science and Engineering, Southwest Jiaotong University, Chengdu 610031, Sichuan, China

2 Yibin Institute of Southwest Jiaotong University, Yibin 644000, Sichuan, China

soften the solid particles and the subsequent introduction of the liquid phase creates a capillary force that pulls them together to increase the density [15]. Besides, samples containing P elements are easy to form attractive circular holes after sintering [16]. Yet, the excessive P element disperses in the matrix with the form of the compound, which plays a role in precipitation strengthening to ensure the strength and toughness of the material [7]. So far, the effect of different Ni–P contents on Fe–Ni–P alloy has not been fully studied. Based on this, this article adopts electroless plating to prepare Fe–Ni–P alloys with various Ni–P contents. The influence of the added content of Ni–P on the microstructure and mechanical properties of Fe–Ni–P alloy is elucidated, which provides a certain value reference for the design of multi-component iron-based alloy materials.

## 2 Experimental

### 2.1 Synthesis process

Fe–Ni–P composite powder was prepared by electroless plating Ni–P on carbonyl iron powder (99.7% purity and 8 μm in average size). The composition of the plating solution is prepared by mixing the reagents in Table 1 with 1 L of distilled water and adjusting pH to 6 ± 0.05 with ammonia water. Then, the selected temperature and time of electroless plating were 75 °C and 1 h, during which stirring was done every 3 min to ensure uniform deposition, and drying was done after completion. Additionally, the different increments of Ni–P in the composite powder are adjusted by controlling the amount of deposited carbonyl iron powder and are expressed by Fe–X(Ni, P). Table 2 reveals the chemical composition of each sample measured by X-ray fluorescence spectrometry (XRF-1800, Japan). The calculated ratio of the content of Ni to P element remains between 6.1–6.8, indicating that the composition of the deposited Ni–P coating (morphology visible [10]) is relatively stable. Furthermore, each powder was put into a stainless steel mold with an inner diameter of 10 mm, an

**Table 1** Composition of electroless plating solution from Jinshan Chemical Test, Chengdu, China, used for deposition

| Composition | Content | Grade |
|---|---|---|
| $NiSO_4 \cdot 6H_2O$ | 30 g | AR |
| $NaH_2PO_2 \cdot H_2O$ | 25 g | AR |
| $CH_3COONa \cdot 3H_2O$ | 15 g | AR |
| $Na_3C_6H_5O_7 \cdot 2H_2O$ | 10 g | AR |
| $C_3H_6O_3$ | 10 mL | AR |
| $NH_3 \cdot H_2O$ | Appropriate | AR |

outer diameter of 20 mm, and a height of 60 mm, respectively, and then pressed into a green compact with a pressure of 10 MPa and kept for 1 min. The mold and the green compact were put into the pit furnace for pressure sintering, and the external force exerted was 2 MPa. According to Ni–P phase diagram [13], the increase in P content causes the liquidus line to decline and the liquid phase content to increase. If there is a large amount of liquid phase, it is easy to form a phosphorus eutectic microstructure, which leads to embrittlement of the interface and deteriorates ductility. Therefore, the sintering temperature is gradually reduced to avoid the formation of eutectic microstructure to a certain extent and then slowly cooled to room temperature with the furnace after holding for 30 min.

### 2.2 Characterization

The actual density of the sample was measured by Archimedes' principle, and the hardness test was carried out on a Vickers hardness tester (HVS-1000, China) with a load of 1 N for 15 s. The phase composition is measured by X-ray diffraction (XRD, X'pert pro, Netherlands) equipped with Cu Kα radiation. The surface morphology and relative element distribution of the samples were observed by optical microscopy (OM, Olympus GX51, Japan) and field emission scanning electron microscopy (FE-SEM, JSM-7800F, Japan) equipped with energy-dispersive X-ray spectroscopy (EDS). The samples of OM and FE-SEM were etched using sodium metabisulfite aqueous solution and ferric chloride plus hydrochloric acid, respectively. All samples are following the ASTM standard in the electronic universal testing machine (WDW-200, China) to complete the compression performance test, where the loading speed is 1 mm/min and the nominal yield strength is determined by 0.2% offset method.

## 3 Results and discussion

The actual density of the final sintered sample has a large difference under different addition amounts of Ni–P, revealing an increasing trend in Fig. 1, and the relative density is 91.40%, 92.10%, 95.63%, 95.47%, and 98.75% in turn. Even if the sintering temperature is relatively high, it is still difficult to obtain the ideal density in samples with low Ni–P content, which may be for Ni–P content in the sintering system is too small to produce an insufficient liquid phase [17]. Since then, with the increase in Ni–P content, while the sintering temperature decreases, the densification curve also rises significantly, and the relative density in Fe–34(Ni, P) sample reaches a peak of 98.75%. It can be seen that with this Ni–P content, the sintering
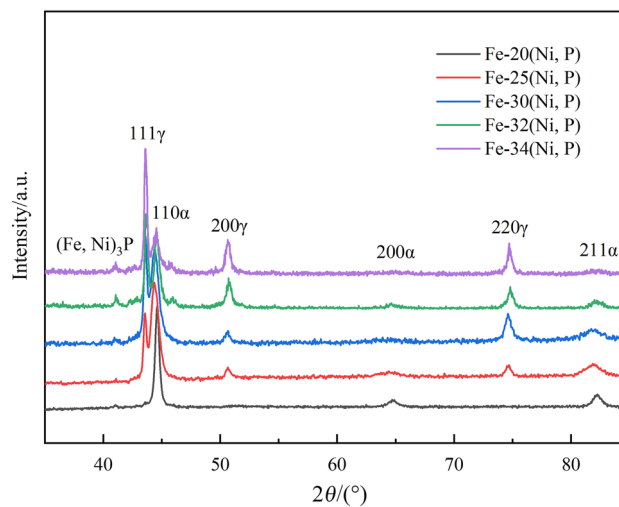
**Table 2** Chemical composition and sintering parameters of Fe–Ni–P composite powder obtained

| Sample ID | Concentration/wt.% | | | | Sintering temperature/°C | Holding time/min |
|---|---|---|---|---|---|---|
| | Fe | Ni | P | Ni + P | | |
| Fe–20(Ni, P) | 77.88 | 17.77 | 2.90 | 20.67 | 975 | 30 |
| Fe–25(Ni, P) | 74.30 | 21.97 | 3.44 | 25.41 | 965 | 30 |
| Fe–30(Ni, P) | 70.80 | 24.97 | 3.97 | 28.94 | 955 | 30 |
| Fe–32(Ni, P) | 67.99 | 27.74 | 4.10 | 31.84 | 945 | 30 |
| Fe–34(Ni, P) | 65.67 | 29.68 | 4.50 | 34.18 | 935 | 30 |
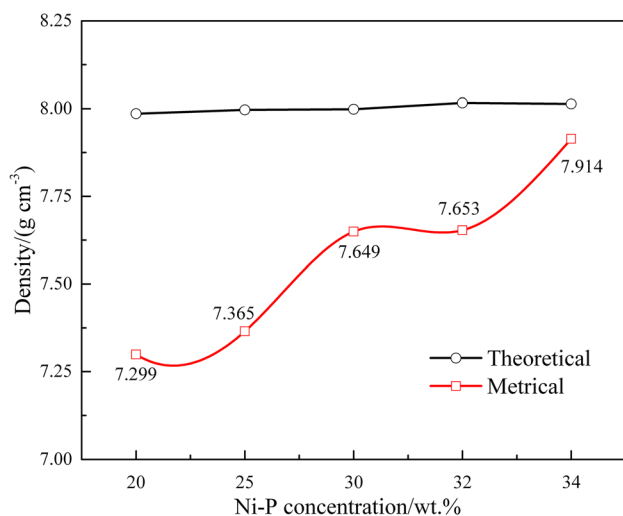


**Fig. 1** Theoretical and metrical density of Fe–Ni–P sintered samples with various Ni–P concentrations



**Fig. 2** XRD spectra of samples with various Ni–P concentrations

temperature and time are sufficient for the densification of the sample. On the one hand, the appearance of the liquid phase effectively promotes the rearrangement of powder particles through lubrication, and on the other hand, it fills up certain voids in the sintering system through flow, thereby significantly increasing the densification rate [15]. At the same time, the solid–liquid phase interacts with each other, as the sintering process progresses until the liquid phase completely disappears and finally becomes solid-phase sintering.

XRD pattern of the sintered sample is shown in Fig. 2. It can be seen that with the increase in Ni–P addition, the main phase of the sample gradually transforms from α to γ phase, and there is a transition zone in the middle, which is consistent with the law reflected in Fe–Ni binary equilibrium phase diagram [18] to a certain extent. And the characteristic peaks of (Fe, Ni)$_3$P phosphide gradually became prominent, revealing that the volume of phosphide increased simultaneously. It is worth noting that when Fe–Ni or Fe–Ni–P alloy is cooled from the high temperature (γ phase) to room temperature, the precipitation of α phase strongly depends on the diffusion of atoms so that a long

aging treatment is required to obtain the equilibrium microstructure reflected in the phase diagram at room temperature [19, 20]. However, the actual cooling rate far exceeds the slow cooling rate required to form the equilibrium microstructure, eventually making α phase inevitably lower than the theoretical value as shown in phase diagram. No characteristic peak of FeNi$_3$ was detected, indicating that the ordering of γ phase is difficult to achieve. Subsequently, γ phase formed at high temperature increases with the increase in Ni content and is not easy to undergo phase transformation during cooling [21]. Therefore, the volume of γ phase in Fe–Ni–P alloy at room temperature directly reflects its stability.

OM and SEM images of sintered samples with different Ni–P levels are shown in Fig. 3, in which the distribution of grain and phosphide is also quite different. Through OM, it can be seen that a large number of bluish-blue areas appear in the samples with relatively low Ni–P content, which are characterized by acicular martensite, and there is fine cryptic martensite dispersed in the grains. With the increase in Ni–P content to 30 wt.%, the matrix is no longer a single yellow–brown, and a well-defined dark brown block appears. No typical martensite morphology was
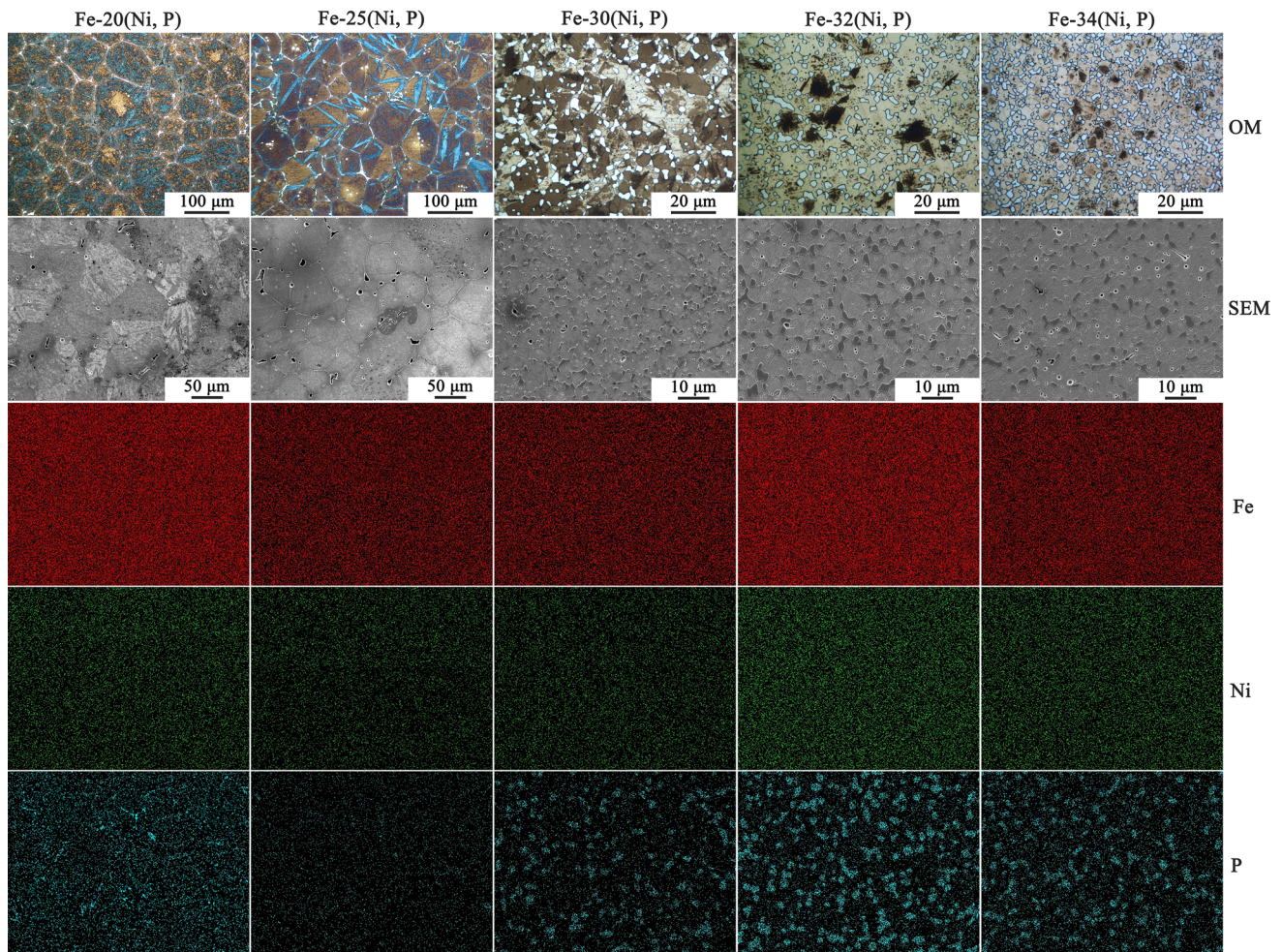
**Fig. 3** OM and SEM microstructure of sintered samples with different amounts of Ni–P as well as element distribution of EDS mapping

observed, while only massive brown areas and white matrix existed, corresponding to α and γ phases, respectively, and the proportion of γ phase increased. Meanwhile, the proportion of α phase is further reduced and a large number of fine phosphides are distributed on the matrix. Phosphide has a strong inhibitory effect on the migration and propagation of the grain boundary, making the grains locally refined, and its distribution changes from a network distribution along the grain boundary to a discrete distribution, avoiding interface embrittlement. And the decrease in sintering temperature also hinders the continuous growth of grain. Then, the grain refinement is gradually saturated, and the grain size is not much different from the initial powder particle size. EDS mapping results of the corresponding elements in the alloy reveal that there is no boundary between the diffusion of Fe and Ni, but the abnormal aggregation of P elements in (Fe, Ni)$_3$P phosphide is obvious, especially in the high Ni–P level. Carefully observing that in Fe–20(Ni, P) sample, the lack of liquid phase promotes element diffusion and particle

rearrangement makes phosphides precipitate along the grain boundaries and form a network, which will cause interface embrittlement to decrease plasticity. In the samples with high Ni–P levels, the phosphide formed in the later stage of sintering no longer precipitates in a network shape as a result of the flow and convergence of the liquid phase. The presence of more liquid phases in the system makes it well contact with the solid Fe particles, thereby having more opportunities for element redistribution.

The transient liquid phase sintering process of Fe–Ni–P composite powder is indicated in Fig. 4. Ni–P coating on the outer layer of iron powder begins to melt as the temperature rises to the liquidus and the element diffusion occurs, which reduces the content of P in the coating and thus reduces the volume of the liquid phase. The resulting liquid phase will fill the pores and promote the rearrangement of the powder particles, thereby significantly increasing the degree of densification. Furthermore, the direction of the liquid phase composition in the area away from the powder surface and the area near the powder
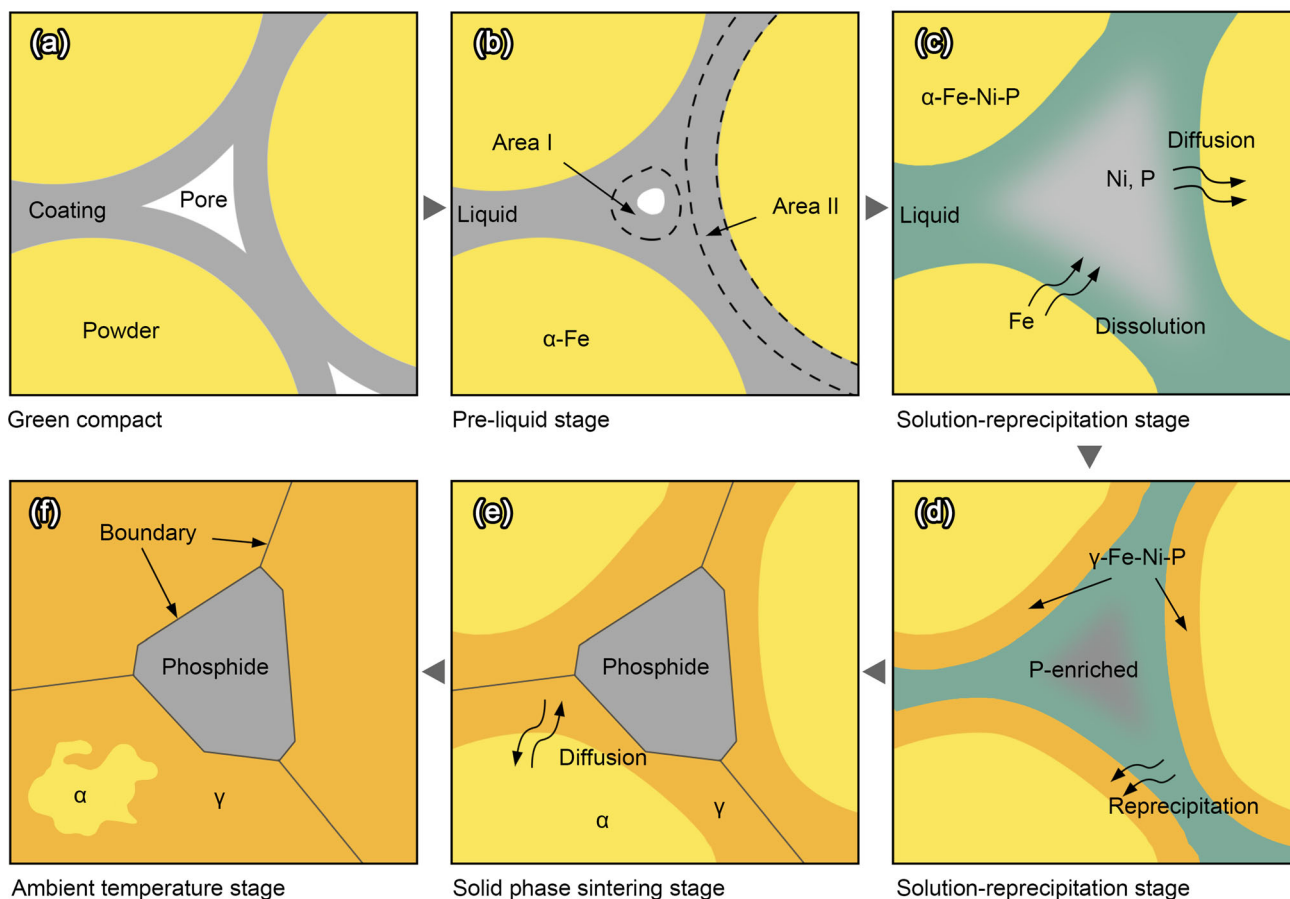
**Fig. 4** Schematic diagram of transient liquid phase sintering process of Fe–Ni–P composite powder

surface begins to change, which are marked as area I and area II in Fig. 4b. First, Fe element in the powder dissolves into the liquid phase, which causes the increase in Fe content and the decrease in P content in the liquid phase, so that the introduction of Fe element in area II should be ahead of that of area I. Subsequently, the content of P in the liquid phase continues to diffuse into the solid phase to further reduce its content, so that the new phase will directly precipitate and form on the surface of the undissolved powder, which significantly accelerates the growth of the sintering neck. If the liquid phase is not completely decomposed during the holding period, a eutectic reaction will occur in the subsequent cooling process, while there is no obvious eutectic microstructure in SEM of Fig. 3. Therefore, it can be inferred that the liquid phase produced is basically consumed through the processes of dissolution and reprecipitation. Finally, the elements in the grains gradually diffuse uniformly during the solid-phase sintering stage and then are cooled to ambient temperature. Finally, a small volume of α phase will be precipitated in the matrix.

The compressive engineering stress–strain curves of samples with various Ni–P contents are given in Fig. 5a.

The compression behavior of the sample indicates a significant transition from hard brittleness to ductile plasticity with the increase in Ni–P level. The sample Fe–20(Ni, P) has a large amount of martensite with low Ni–P content, which makes it exhibit the highest yield strength of 1255.6 MPa. Nevertheless, the internal pores fail to achieve sufficient densification, and the presence of martensite plus the phosphide distributed along with the network results in poor plasticity. The increase in Ni–P content is accompanied by an increase in the proportion of γ phase in the matrix, which significantly adjusts the mechanical properties so that the plasticity gradually increases while the relative strength reveals a downward trend. The sample Fe–34(Ni, P) has the lowest yield strength of 600.1 MPa and demonstrates the most obvious strain hardening behavior under the maximum applied load. This is because more γ phase formed by higher Ni content (austenite stabilizer) is prone to martensitic transformation under stress, leading to delayed fracture [22]. Phase transformation strengthening is easier to be obtained when the amount of deformation is larger, which makes the overall deformation of the sample more uniform and thus less likely to produce strain concentration [23, 24]. What is
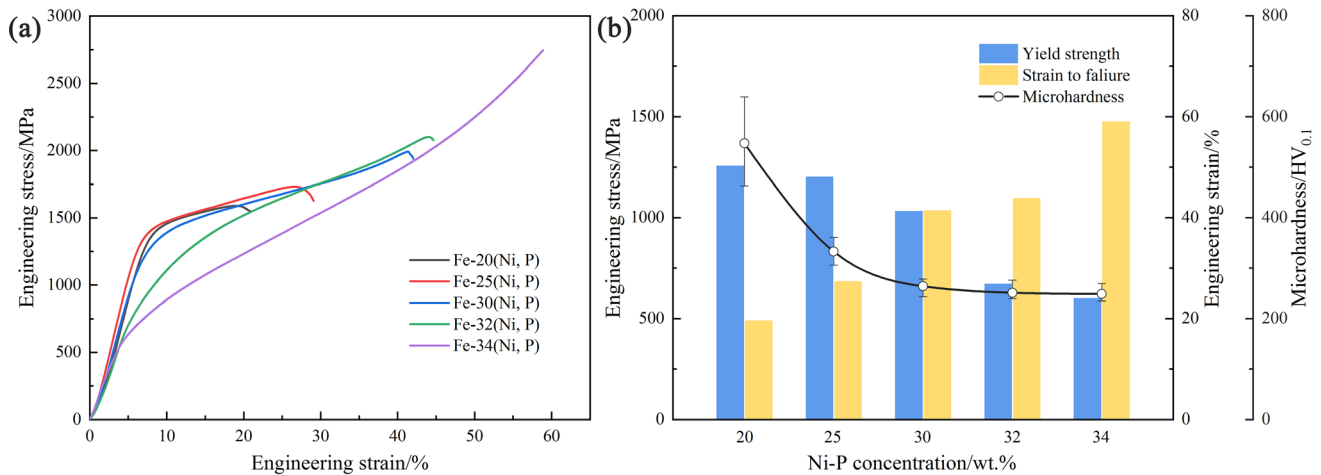
Fig. 5 Mechanical properties of samples under different contents of Ni–P. **a** Compression engineering stress–strain curve; **b** mechanical behavior parameters

more, $\gamma$ phase is not as unstable as possible but needs to maintain a certain degree of stability, so that the degree of phase change will increase synergistically with the increase in the applied load to achieve the best plasticizing effect.

Figure 5b reveals the different mechanical properties of each sample, where the changing trend of hardness is similar to the yield strength. The hardness reaches the peak of 547 $HV_{0.1}$ at the lowest Ni–P addition, but then the hardness decreases significantly with the increase in its content, and gradually stabilizes after reaching a certain level. This is due to the existence of several counter-balance mechanisms in the sample. On the one hand, the decrease in the proportion of $\alpha$ phase will weaken the hardness and yield strength of the material, and on the other hand, the refinement of grains and the increase in hard and brittle phase phosphide are factors that increase the hardness and yield strength of materials. The reduction of $\alpha$ phase in the low Ni–P level has a more significant weakening effect on the strength of the material, while in the high Ni–P level, the volume of $\alpha$ phase has been reduced to a relatively stable level; the effect of the first mechanism tends to be saturated and then the effect of the second mechanism can be reflected.

The fracture surface shown in Fig. 6 can more intuitively reflect the scene during compression. From the low Ni–P level samples in Fig. 6a, b, it can be seen that their fracture surfaces are uniformly showing a typical river pattern, and the surface is smooth and basically without dimples, that is, brittle fracture occurs. The surface morphology in Fig. 3 indicates that the precipitation of (Fe, Ni)$_3$P phosphide along the grain boundary greatly weakens the intergranular bonding force, which is also closely related to their similar high strength and low plasticity. With the gradual increase in Ni–P content, a mixed mode of ductile and brittle fracture appears in Fig. 6c–e.

Although there is a small range of lamellar cleavage surfaces, there are still certain dimples, which corresponds to its excellent ductile.

## 4 Conclusions

1. The actual density of the final sintered sample shows an increasing trend with the increase in Ni–P content and its relative density reaches a peak of 98.75% in the sample Fe–34(Ni, P). This can be attributed to the fact that the appearance of the liquid phase effectively promotes the rearrangement of powder particles through lubrication and fills up certain gaps through its fluidity.

2. The main phase of the sample gradually changed from $\alpha$ to $\gamma$ phase with the increase in Ni–P content, and the distribution law of (Fe, Ni)$_3$P phosphide evolved from network distribution along grain boundary to discrete distribution. A large number of phosphides that have strong inhibition on the migration and expansion of grain boundaries are precipitated on the matrix and synergistic effect with low-temperature sintering results in partial grain refinement.

3. As the content of Ni–P increases, the compressive behavior of the sample indicated a significant transition from hard and brittle to ductile and plastic. The sample Fe–20(Ni, P) exhibits the highest strength, namely, the yield strength and microhardness of 1255.6 MPa and 547 $HV_{0.1}$, respectively. Sample Fe–34(Ni, P) with higher Ni–P content exhibited excellent phase transformation strengthening effect during compressive strain because of their higher volume of $\gamma$ phase. And the fracture mode has also

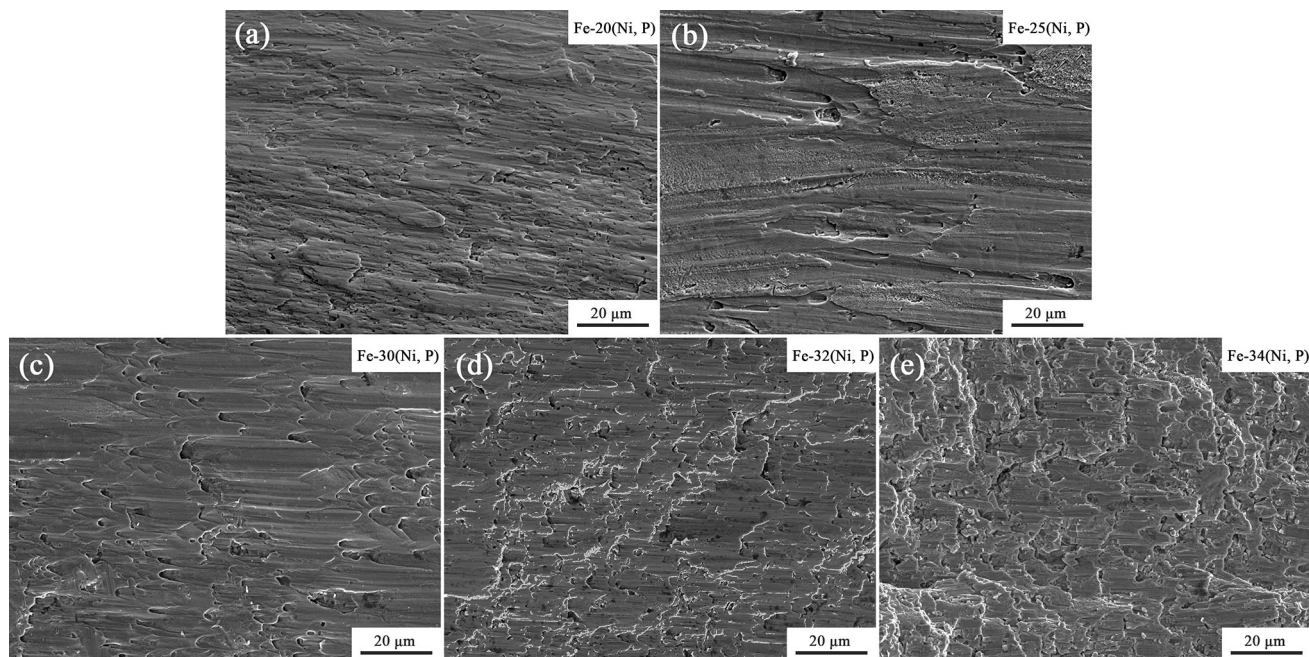**Fig. 6** Compressed fracture morphology of various samples

changed from brittle fracture to a mixed mode of brittle and ductile fractures.

# References

[1] M. van Schilfgaarde, I.A. Abrikosov, B. Johansson, Nature 400 (1999) 46–49.

[2] D.C. Jiles, Acta Mater. 51 (2003) 5907–5939.

[3] H. Kotan, M. Saber, C.C. Koch, R.O. Scattergood, Mater. Sci. Eng. A 552 (2012) 310–315.

[4] P. Ripka, J. Magn. Magn. Mater. 320 (2008) 2466–2473.

[5] B. Zhang, N.E. Fenineche, H. Liao, C. Coddet, J. Mater. Sci. Technol. 29 (2013) 757–760.

[6] H.R. Ren, J.T. Gao, Z. Wang, C. Li, F.Q. Wang, Z.C. Guo, J. Iron Steel Res. Int. 24 (2017) 844–851.

[7] W. Chai, R.M. German, E.A. Olevsky, X. Wei, R. Jiang, G. Cui, Adv. Eng. Mater. 18 (2016) 1889–1896.

[8] L. Zhong, R. Wu, A.J. Freeman, G.B. Olson, Phys. Rev. B 55 (1997) 11133–11137.

[9] S.L. Yang, W.R. Sun, F. Liu, S.R. Guo, H.C. Yang, Z.Q. Hu, J. Iron Steel Res. Int. 15 (2008) No. 3, 61–64.

[10] R. Jiang, A. Li, G. Cui, C. Zhang, Metall. Mater. Trans. A 50 (2019) 2580–2584.

[11] Y.D. He, H.F. Fu, X.G. Li, W. Gao, Scripta Mater. 58 (2008) 504–507.

[12] Y. Yang, S. Liu, J. Li, X. Bian, Z. Guo, Surf. Coat. Technol. 315 (2017) 484–489.

[13] H. Okamoto, J. Phase Equilib. 21 (2000) 210.

[14] E.A. Olevsky, Mater. Sci. Eng. R Rep. 23 (1998) 41–100.

[15] R.M. German, P. Suri, S.J. Park, J. Mater. Sci. 44 (2009) 1–39.

[16] K. Hwang, K. Lin, Powder Metall. 35 (1992) 292–299.

[17] J. Svoboda, H. Riedel, R. Gaebel, Acta Mater. 44 (1996) 3215–3226.

[18] L.J. Swartzendruber, V.P. Itkin, C.B. Alcock, J. Phase Equilib. 12 (1991) 288–312.

[19] J.I. Goldstein, A.S. Doan, Geochim. Cosmochim. Acta 36 (1972) 51–60, IN3–IN8, 61–69.

[20] A.D. Romig, J.I. Goldstein, Geochim. Cosmochim. Acta 45 (1981) 1187–1197.

[21] L. Kaufman, M. Cohen, JOM 8 (1956) 1393–1401.

[22] X.M. Zhang, D.F. Li, Z.S. Xing, E. Gautier, J.S. Zhang, A. Simon, Acta Metall. Mater. 41 (1993) 1693–1699.

[23] Z. Li, C.C. Tasan, K.G. Pradeep, D. Raabe, Acta Mater. 131 (2017) 323–335.

[24] P.C. Maxwell, A. Goldberg, J.C. Shyne, Metall. Mater. Trans. B 5 (1974) 1305–1318.